Contributions to Geophysics and Geodesy Vol. 51/2, 2021 (165–188)

Deformation-induced topographic effect due to shallow dyke: Etna December 2018 fissure eruption case study

Peter VAJDA[1,*], Pavol ZAHOREC[1], Juraj PAPČO[2], Richard CZIKHARDT[2]

[1] Earth Science Institute, Slovak Academy of Sciences, Dúbravská cesta 9, P.O.Box 106, SK-840 05, Bratislava, Slovak Republic

[2] Dept. of Theoretical Geodesy and Geoinformatics, Slovak University of Technology, Radlinského 11, SK-810 05 Bratislava 15, Slovak Republic

Abstract: Gravitational effect of surface deformation is in 4D microgravimetry treated as the deformation-induced topographic effect (DITE). The DITE field is computed using Newtonian volumetric integration which requires high resolution digital elevation model (DEM) and vertical displacement field in areal form. If only elevation changes on benchmarks of the gravimetric network are available, instead of the vertical displacement field, the DITE on benchmarks can be evaluated only approximately, using a planar Bouguer or a normal free-air-effect (nFAE) approximation. Here we analyse the adequacy and accuracy of these two approximations in a case study for the December 2018 fissure eruption on Etna accompanied by significant surface deformation caused primarily by a relatively shallow dyke. The outcome is that in volcanic areas of similar morphology as that over the Etna summit area, and for surface deformation fields due to relatively shallow dykes, neither the Bouguer nor the nFAE approximation of the DITE is accurate enough. In such situations the residual gravity changes should be computed with both the Bouguer and nFAE corrections and interpreted as two marginal cases. In addition we analyse also a correction for the effect of benchmark elevation change based on the topographically modelled (predicted) vertical gradient of gravity (VGG) meant to approximate the in-situ VGG values at benchmarks. This correction does not appear suitable to approximate the DITE in conditions of our case study or in broader sense.

Key words: volcano geodesy, 4D microgravimetry, spatiotemporal gravity change, DITE, surface deformation

1. Introduction

Spatiotemporal (time-lapse) gravity changes observed in volcanic areas are complex composite signals. The observed gravity changes (Δg) must be

*corresponding author: e-mail: Peter.Vajda@savba.sk, ORCID: 0000-0001-9046-480X, SCOPUS ID: 7005183079

doi: 10.31577/congeo.2021.51.2.4

first corrected for all signal components other than those associated with the studied volcanic processes (e.g., *Battaglia et al., 2008; Carbone et al., 2017; Fernández et al., 2017; Van Camp et al., 2017*). Among these are atmospheric and tidal effects, instrumental and survey design effects, and hydrological effects. For a review of these effects and their treatment see (*Vajda et al., 2019* and references therein).

If elevation changes, i.e. surface vertical displacements (Δh), accompany gravity changes then the gravitational effect of the surface deformation must be carefully corrected for. To extract the gravitational signal component related only to the mass and/or density changes related to the source (Δg^{M}), several gravitational effects must still be removed. This removal of unwanted signal components constitutes the computation of residual gravity changes Δg^{res} (e.g., *Vajda et al., 2019, 2021*):

$$\Delta g^{\mathrm{res}}(P) \equiv \Delta g(P) - \Delta g^{\mathrm{FAE}}(P) - \Delta g^{\mathrm{sdef}}(P) - \Delta g^{\mathrm{idef}}(P) = \Delta g^{\mathrm{M}}(P)\,. \quad (1)$$

The individual signal components, evaluated at the gravity benchmark on the (post-deformation) topographic surface (P) are as follows. The Δg^{FAE} term is the so called free-air effect (FAE). It is the gradient effect based on the true (in situ) vertical gradient of gravity (VGG). The FAE is due to the vertical displacement of the gravity benchmark in the ambient gravity field, i.e. in free-air, disregarding the fact that the topographic masses attached to the deformed surface are moving along with the displaced surface.

The latter effect is treated as the attraction of surface deformation (Δg^{sdef}). The Δg^{sdef} term is a sum of two terms: (1) the attraction of topographic masses enclosed between the pre- and post-deformation topographic surfaces, referred to as the Topographic Deformation Effect (Δg^{TDE}), and (2) the attraction of surface mass changes, such as outpoured cooled lava flows, fall-out products, morphological dome changes, lahars, flank collapses, debris accumulations, etc. (Δg^{surf}), both the terms being discussed in (*Vajda et al., 2019*). Since both attractions are evaluated by the same numerical volumetric integration for points on the post-deformation topographic surface, it does not make sense to distinguish between them. Instead, they can be computed together as one term (Δg^{sdef}). Due to the relief of the topographic surface, the Δg^{sdef} term must be numerically evaluated by 3D Newtonian volumetric integration.

The Δg^{idef} term is the attraction of inner deformations (structural ones

and those related to the source boundary). While the attraction of surface deformation (Δg^{sdef}) can be computed from the observable surface deformation (and observable surface mass changes), and applied as a correction to observed gravity changes, the attraction of inner deformations can only be estimated or modelled.

We stress that the terms Δg^{FAE} and Δg^{sdef} should never be treated numerically separately. The reason is that both terms contain a highly variable short-wavelength signal due to the relief of the topographic surface, and their sum should be treated as one term, named the Deformation-Induced Topographic Effect (DITE):

$$\Delta g^{\mathrm{DITE}}(P) \equiv \Delta g^{\mathrm{FAE}}(P) + \Delta g^{\mathrm{sdef}}(P)\,, \tag{2}$$

in which the highly variable short-wavelength signal is significantly suppressed. Here, the free-air effect (FAE) is based on the VGG (Γ) observed at the benchmark, by which the elevation change (Δh) of a benchmark is multiplied:

$$\Delta g^{\mathrm{FAE}}(P) = \Gamma(P)\,\Delta h(P)\,. \tag{3}$$

The second DITE constituent (Δg^{sdef}), the attraction of surface deformation must be computed by a 3D Newtonian volumetric integration. The conceptual (defining) expression of DITE, Eq. (2), is not well suited for the numerical evaluation of DITE, as it demands the measurement of VGG at each benchmark, which is not always possible. Moreover, even if measured VGG values were available at benchmarks, it would be very difficult to compute the Δg^{sdef} term accurately due to the limited accuracy of the DEM (DTM) and the lack of the knowledge of the real near-surface rock density. Therefore, *Vajda et al. (2019)* have derived an expression much more suitable for the numerical realization of DITE defined by Eq. (2), omitting the measurement of the real VGG, as well as minimizing the issues related to the accuracy of evaluating the Δg^{sdef} term:

$$\Delta g^{\mathrm{DITE}}(P) = \Gamma_0 \Delta h(P) + \left[a^{\mathrm{T}*}(P^*) - a^{\mathrm{T}}(P)\right]. \tag{4}$$

This new expression is called "quasi exact DITE" (qeDITE) and represents the most accurate approximation of DITE under the assumption of constant reference topographic density (neglecting the effects of density anomalies on DITE). It replaces the use of VGG in DITE by the use of

the constant gradient of normal gravity (Γ_0). In qeDITE the first term is a gradient effect, this time based on the constant theoretical (normal) free-air gradient (FAG), $\Gamma_0 = -308.6\,\mu$Gal/m ($1\,\mu$Gal/m $= 10^{-8}\,\mathrm{s}^{-2}$). The square brackets term constitutes the difference between the attraction of the post-deformation topographic masses evaluated on the post-deformation topographic surface ($a^{\mathrm{T}*}(P^*)$) and the attraction of the pre-deformation topographic masses evaluated on the pre-deformation topographic surface ($a^{\mathrm{T}}(P)$). This is not the same as the attraction of masses trapped between pre- and post-deformation surfaces. The topographic masses are those bound between sea level and the earth surface. A constant reference density (ρ_0) of the topographic masses is adopted in evaluating this term. The square brackets term is evaluated by numerical volumetric Newtonian integration, which requires an accurate and high-resolution digital elevation model (DEM) of the study area, ideally with horizontal resolution less than 10 m and vertical accuracy better than 10 cm, a correct choice of the topographic reference density (ρ_0), and the availability of the vertical displacement field in areal form.

Vertical displacements in areal or grid form can be provided by Differential Interferometric Synthetic Apperture Radar (DInSAR), by repeat Light Detecting And Ranging (LiDAR) measurements, or by repeat photogrammetric observations (e.g., *Fornaciai et al., 2010; Diefenbach et al., 2012, 2013; Aldeghi et al., 2019; Carr et al., 2019; Jordan, 2019; Okyay et al., 2019*). For the numerical evaluation of the square brackets term in Eq. (4) we use the software Toposk (*Zahorec et al., 2017*) which calculates the attraction of topographic masses up to the distance of the outer limit of zone O (166.7 km) of the Hayford-Bowie system (*Hayford and Bowie, 1912*). Different resolution DEMs, with resolution increasing towards the evaluation point, and different representations (with the option of using planar or spherical approach) of the volumetric elements are used within different integration zones of the Hayford-Bowie system.

If the vertical displacements are only available as scattered point data at gravity benchmarks, then the DITE can be evaluated only approximately by multiplying the elevation change at each benchmark by some sort of gravity gradient value. The question arises which gradient value is to be used. Should one use in-situ VGG measured at each benchmark, or, if not available, its approximation by the topographically-predicted VGG (*Vajda*

et al., 2020)? Should the constant theoretical (normal) FAG be used, or the Bouguer-corrected FAG (BCFAG)? Or do different conditions or situations require the use of different values of the vertical gradient? *Vajda et al. (2019)* addressed this question by performing numerical simulations of the DITE respective to various size and shape deformation fields imposed over relief features of various shapes. The outcome of their study is that most commonly the Bouguer approximation (BCFAG-DITE) would perform the best. It uses the planar BCFAG (Γ_{B}), cf. (e.g., *Berrino et al., 1984, 1992; Rymer, 1994*):

$$\Delta g^{\mathrm{DITE}}(P) \approx \Gamma_{\mathrm{B}}\, \Delta h(P)\,, \quad \text{where } \Gamma_{\mathrm{B}} = [\Gamma_0 + 2\pi G \rho_0]\,, \tag{5}$$

where G is the Newton constant and Γ_0 is the constant theoretical (normal) FAG. However, under particular conditions the "normal FAE" (nFAE):

$$\Delta g^{\mathrm{DITE}}(P) \approx \Gamma_0\, \Delta h(P) \tag{6}$$

will become a better approximation of DITE. The numerical simulations revealed that the physical nature of DITE varies between two limiting cases: the nFAE-DITE and the BCFAG-DITE. The DITE varies depending on the shape, lateral extent and amplitude of the deformation field, as well as the shape of the relief over which it is imposed. In flatter or less rugged relief the nature of DITE is closer to its Bouguer representation (Eq. (5)). In special cases of short-wavelength deformation fields (such as those generated by shallow small spherical sources or by vertically elongated shallow sources) imposed over steep cone-shape terrain the nature of DITE is closer to its normal-free-air representation (Eq. (6)).

Some 4D microgravimetric studies on volcanoes (*Bonaccorso et al., 2011; Greco et al., 2012; Bonforte et al., 2017* and others) prefer the use of the FAE correction (Eq. (3)). If the VGG values at benchmarks are not available (were not observed), they can be, in areas of rugged topographic relief, successfully approximated by their topographically predicted (modelled) values (Γ_P), see *Zahorec et al. (2016), Vajda et al. (2020).* Just for the sake of completeness, we shall numerically compare to the DITE field also the field computed as the predicted VGG field times the vertical displacement field:

$$\Delta g^{\mathrm{DITE}}(P) \approx \Gamma_P(P)\, \Delta h(P)\,, \tag{7}$$

to see whether it would be suitable to approximate the DITE.

In other volcano gravimetric studies the value of the VGG on benchmarks is replaced by a locally estimated constant value of the VGG (e.g., *Miller et al., 2017*). The deviation of such treatment of the gravitational effect of surface deformation from the DITE and its impact on the interpretation of the residual gravity changes was assessed in a case study for Laguna del Maule, Chile by *Vajda et al. (2021).*

In this study we focus on approximating the DITE in volcanic areas with morphologies similar to that of the upper part of Mount Etna, in cases of surface deformation caused by shallow dykes. We use a case study representing the December 2018 fissure eruption on Etna, which was accompanied by significant surface deformation with a range of vertical displacements (from subsidence to uplift) of ca. 30 cm. The shallow dyke, as a primary source of the surface deformation accompanying this volcanic (and seismic) event, was inferred by inverse analytical modelling (*Bonforte et al., 2019; De Novellis et al., 2019*).

We compare the DITE field (Eq. (4)) with its Bouguer approximation (Eq. (5)) in section 2.4, its normal-free-air approximation (Eq. (6)) in section 2.5, and finally with the field obtained by multiplying the vertical displacement field by the topographically predicted (modelled) VGG field (Eq. (7)) in section 2.6.

2. DITE case study for Etna eruption of 24–27 December 2018

2.1. Fissure eruption of Dec-2018

The eruption of 24 December 2018 (*Calvari et al., 2020*) is one of the significant recent eruptions of Etna volcano, Sicily (Fig. 1). It was preceded by two years of ground uplift at a nearly constant rate (*Chauhan et al., 2020*) and by increasing explosive and effusive activity at the summit craters during the last few months before the main eruption. A shallow (1–2 km) seismic swarm of low-magnitude volcano-tectonic events occurred beneath the southeastern flank of the volcano in the morning of 24 December (*Alparone et al., 2020*). An hour later, the summit GPS stations started recording ground deformation (*Cannavò, 2019*). The ground displacement culminated at noon, when a nearly 3 km long eruptive fissure opened at the base of the New South-East Crater (NSEC) and along the western flank of the Valle

Fig. 1. Geographical location of Etna volcano.

del Bove (*Bonforte et al., 2019*). Strong Strombolian activity and several lava flows occurred along the eruptive fissure (*Laiolo et al., 2019*). Activity along the eruptive fissure lasted until 27 December. Sentinel-1 interferograms show a wide and intense ground deformation with some additional features related to volcano-tectonic structures.

The 24–27 December 2018 Etna eruption represents a peculiar paroxysmal event. The bulk of the eruption-related ground deformation developed in a matter of hours (*Cannavò et al., 2019*) and was driven by a ~ 1 m spreading of the volcano edifice and underlying sedimentary basement, across a depth range of some kilometers (*Bonforte et al., 2019; De Novellis et al., 2019*). Results of previous studies (*Chauhan et al. 2020; Bonforte et al., 2019; De Novellis et al., 2019*) indicate that the observed syn-eruptive deformation was associated with a bulk volume increase of some tens of millions cubic meters, while the erupted volume (effusive activity) amounted to only about 1×10^6 m^3 (*Laiolo et al., 2019*).

Studies interpreting the surface deformation of this eruption derived from InSAR data (*Bonforte et al., 2019; De Novellis et al., 2019*) inferred composite (multisource) dyke models. The interpreted syn-eruption surface deformation field is respective to a 6-day Sentinel-1 interval (22–28 December). The deformation field therefore contains besides the signal of the tensile dislocation due to the intrusion of the feeder dyke, also other (second order) deformation effects related to volcano-tectonic structures.

Bonforte et al. (2019) inverted the Sentinel-1 (S1) DInSAR data in the summit area of Mount Etna to characterize the magma intrusion. In their inverse modelling, using optimization routine based on the Genetic Algorithm approach, they searched for dislocation sources (Okada sources) and deflation (depressurizing) sources (Yang-source). Their resulting model indicates that a large dyke intruded up to about the sea level. This big intrusion allegedly stretched the edifice, promoting the opening of the eruptive fissures fed by a shallower small dyke, and activated also several faults. Their solution consists of four deformation sources: (1) a shallow small dyke (Okada shallow dyke) extending from the summit area SE-ward for about 2.5 km, with a depth span ca. 500–1500 m a.s.l, with a slip of 1 m and opening of 1 m, (2) a deeper bigger vertical dyke (Okada deeper dyke), N–S oriented, about 6.3 km long and 3.8 km wide, with depth of its top at 2.5 km, opening of 1.3 m and slip 30 cm, (3) a dislocation source (Okada FF dislocation source) at the Fiandaca fault, and (4) a depressurizing source (Yang pressure source) at the depth of ca. 6 km below sea level, centered below the deeper dyke.

De Novellis et al. (2019) also interpreted DInSAR data. The vertical displacement field in the summit area shows a general subsidence of the western sector of the summit. The most localized deformation pattern identified corresponds to La Montagnola area and shows a subsidence of 15 cm, whereas, to the east, 28 cm of uplift is revealed. *De Novellis et al. (2019)* inferred a similar magma injection source utilizing a dyke intrusion and a shallower dyke feeding the fissure eruption. In their analytical inverse modelling they used shear and tensile dislocation sources. Their model retrieves two dykes. One nearly vertical dyke vertically elongated for about 4.4 km, with a maximum opening of ~ 1.2 m, horizontally matching the location of the vents and of the ground fractures observed in the field. The other nearly vertical dyke extends southward in the area of La Montagnola to 8.5 km depth, with a maximum opening of 95 cm.

Chauhan et al. (2020) model jointly the surface deformations (GPS data at 30 of the 39 cGPS network stations for a period 23–26 December) and gravity changes (at two superconducting gravity observation sites MNT and SLN) using a dyke opening (tensile dislocation) source. They conclude that a more complex mechanism, likely involving the formation of new void space through local increase of the fracturing rate of the medium, rather than a

mere dyke injection, led to the breakout of the December 2018 eruption.

Bonaccorso and Giampiccolo (2020) also report a two dykes ("double dyke") source (cf. their Fig. 3), inferred by *Aloisi et al. (2020)*, cf. their Fig. 12. *Aloisi et al. (2020)* jointly analysed and modelled different types of continuous deformation data (strainmeters, tiltmeters and high-rate GPS) to constrain a detailed and complete model and the time evolution for the December 24–25, 2018 eruptive intrusion. The shallower dyke, commencing at 3 km below the summit craters area, gradually increased its horizontal dimension. It began propagating on December 24 at 8:20, reached the ground surface at 11:10 and fed the short-lived fissure eruption. After the start of the eruption and until the afternoon of December 25, a second deeper dyke penetrated the high southern eastern flank but did not reach the surface. This non-eruptive dyke was very thick (~ 5 m opening) and deeper, departing from about 3 km b.s.l. and stopping inside the volcano edifice at 1.5 km a.s.l. without surfacing.

2.2. Vertical displacement field

In our case study we use the vertical displacement field respective to the 24 Dec 2018 fissure eruption on Etna derived from Sentinel-1 (S1) SAR data. The data over Etna comprise the ascending (Track 44) and descending (Track 124) passes with a 6-day revisit time, acquisitions of 22 and 28 December 2018. For DInSAR processing we use ESA SNAP software (+ SNAPHU), applying the following steps on Sentinel-1 ASC and DSC SLC data: inclusion of the precise orbits, necessary data preparation (split of the bursts), back-geocoding (DEM-assisted) co-registration utilizing SRTM 1sec DEM, complex data resampling making use of 5-point bi-sinc interpolation, bursts merging, interferogram formation, subtraction of flat-earth phase and topographic phase (SRTM 1sec DEM) plus coherence estimation (7×7 window), multi-looking with 7 looks in range and 2 azimuthal looks, Goldstein phase filtering (adaptive filter exponent 0.4, FFT window size 64 pix, window size 3 pix) with coherence mask (0.2 threshold), phase unwrapping with SNAPHU (MCF) based on (*Chen and Zebker, 2000*), phase-to-displacement conversion in line-of-sight (LOS) direction, masking with coherence (0.4). Displacement (in LOS direction) was consequently interpolated to regular 1 sec grid using Kriging. Resultant displacement fields were zero-referenced

w.r.t. reference point MNT (Montagnola). ASC 44 and DSC 124 based regular interpolated displacement data were used for decomposition from LOS direction displacement into vertical and east-west displacement components (*Ketelaar, 2009*). The vertical displacement field is shown in Fig. 2.

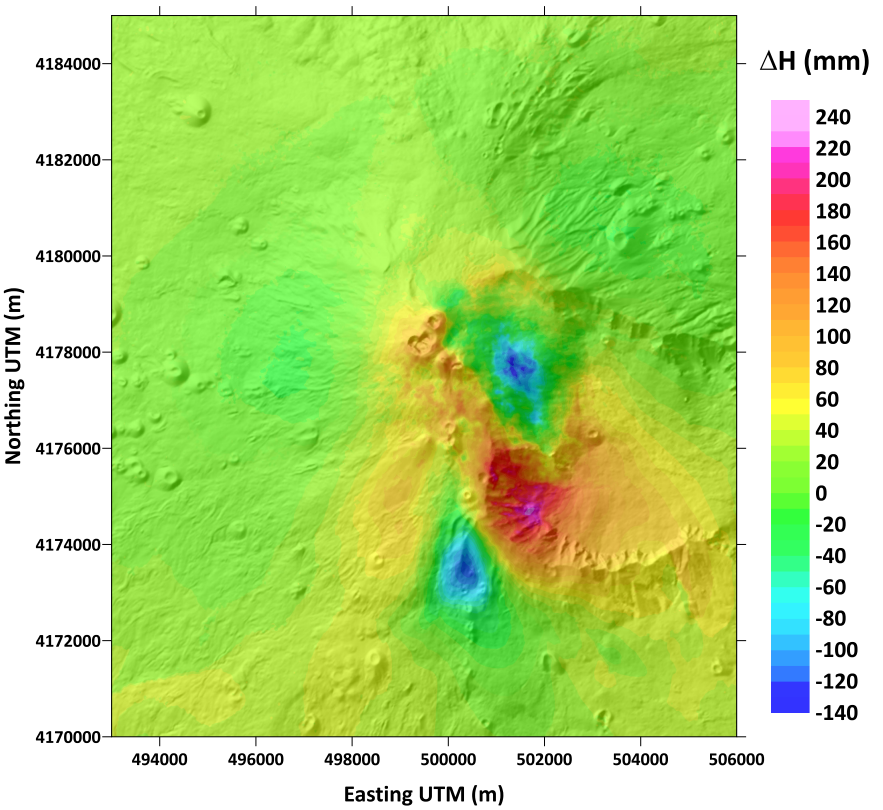

Fig. 2. The syn-eruptive vertical displacement field (mm) of the Dec-2018 fissure eruption on Etna derived from DInSAR (Sentinel-1, 22–28 Dec 2018) draped over shaded relief of Etna.

2.3. DITE field

To compute the DITE accurately (Fig. 3), the square brackets term in Eq. (4) is evaluated by numerical volumetric Newtonian integration, which requires an accurate and high-resolution DEM of the study area for the integration in the innermost zone, and the vertical displacement field. We used the Li-

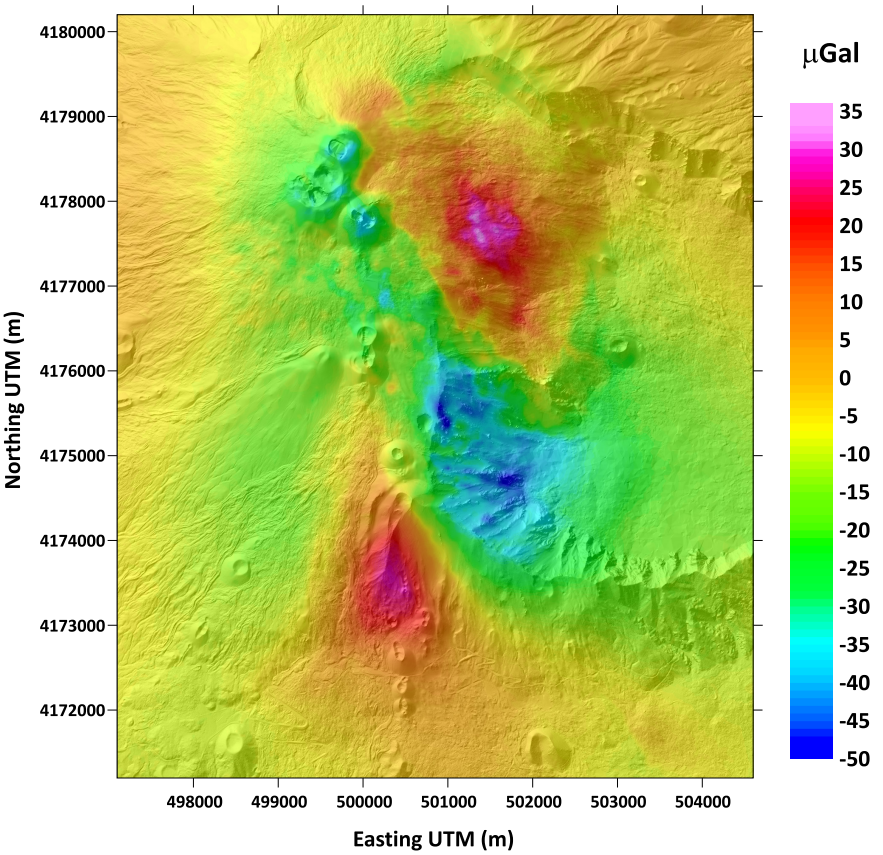

Fig. 3. Syn-eruptive DITE field of the Dec-2018 fissure eruption on Etna (μGal) respective to the surface deformation shown in Fig. 2.

DAR DTM 2005 (*Bisson et al., 2016*) with the resolution of 5 m and vertical accuracy (rms) of 24 cm as the best available DEM in our study area. The correct choice of the topographic reference density (ρ_0) for evaluating the square brackets term is important, too. We used the value of 2670 kg/m^3 (*Schiavone and Loddo, 2007*). We used the vertical displacement field shown in Fig. 2.

For the numerical evaluation of the square brackets term in Eq. (4) we use the software Toposk (*Zahorec et al., 2017*) which calculates the attraction of topographic masses up to the distance of the outer limit of zone O (166.7 km) of the Hayford-Bowie system (*Hayford and Bowie, 1912*). Differ-

ent resolution DEMs (increasing towards the evaluation point) and different representations (with the option of using planar or spherical approach) of the volumetric elements are used within different integration zones of the Hayford-Bowie system.

2.4. Bouguer approximation of DITE

The DITE computation requires numerical volumetric integration similar to the computation of the terrain or topographic correction in gravimetry. If the deformation field is not available in areal (grid) form, then the

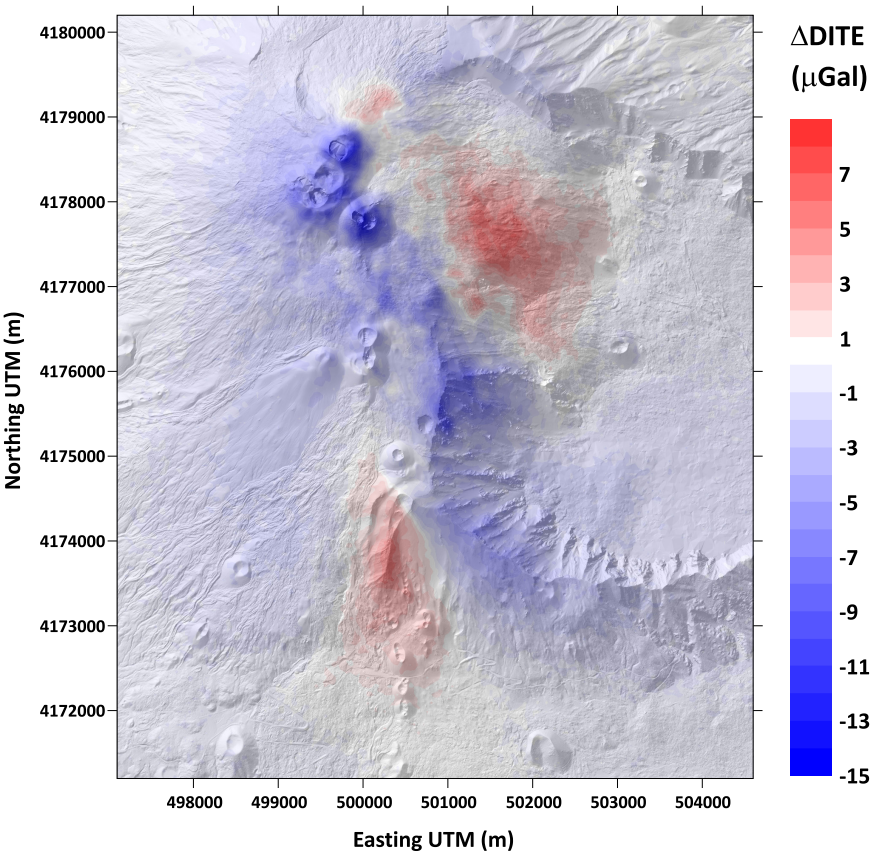

Fig. 4. The difference (μGal) between the DITE field and its Bouguer approximation for the vertical displacement field shown in Fig. 2.

DITE can be approximated by multiplying the elevation changes observed at gravity benchmarks by a constant value of the Bouguer corrected FAG (BCFAG), cf. Eq. (5). The BCFAG value depends on the topographic density chosen to represent the study region. We used a density of 2670 kg/m^3 (*Schiavone and Loddo, 2007*). For this density the value of the BCFAG is -197 μGal/m.

In Figure 4 we compare the DITE field with the planar Bouguer approximation of the DITE field by showing their difference. Over the whole study area the statistics of the difference between the two fields are: min = -14.5 μGal, max = 7.5 μGal, mean = -1.1 μGal, and RMS = 2.3 μGal.

In Figure 5 we show the difference of Figure 4 in a relative sense as this

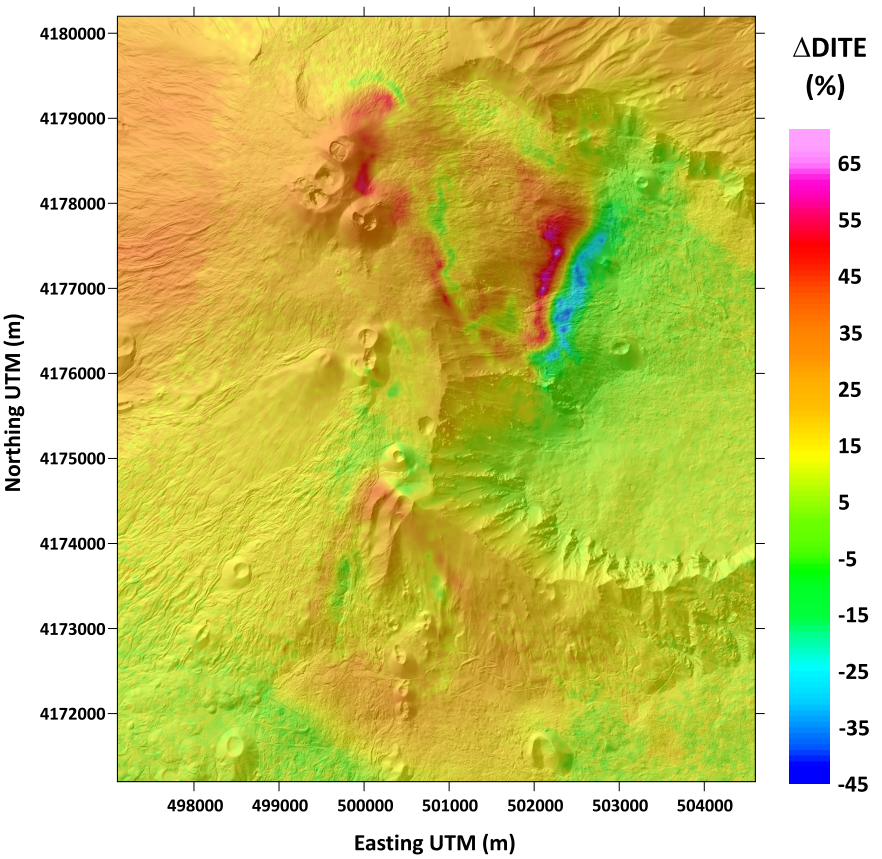

Fig. 5. The difference shown in Fig. 4 presented in relative sense (%).

difference divided by the DITE. We do this only for the grid (mesh) points where the DITE signal (in absolute sense) is greater than 5 μGal, to avoid values of several hundred percent for spots where the DITE is very small. This relative difference is interpolated over the empty spots where the DITE signal (in absolute sense) is less than 5 μGal.

2.5. Normal Free-Air approximation of DITE

Just as we compared the Bouguer approximation of DITE to the actual DITE field in the above section, here we do the same (Fig. 6) for the

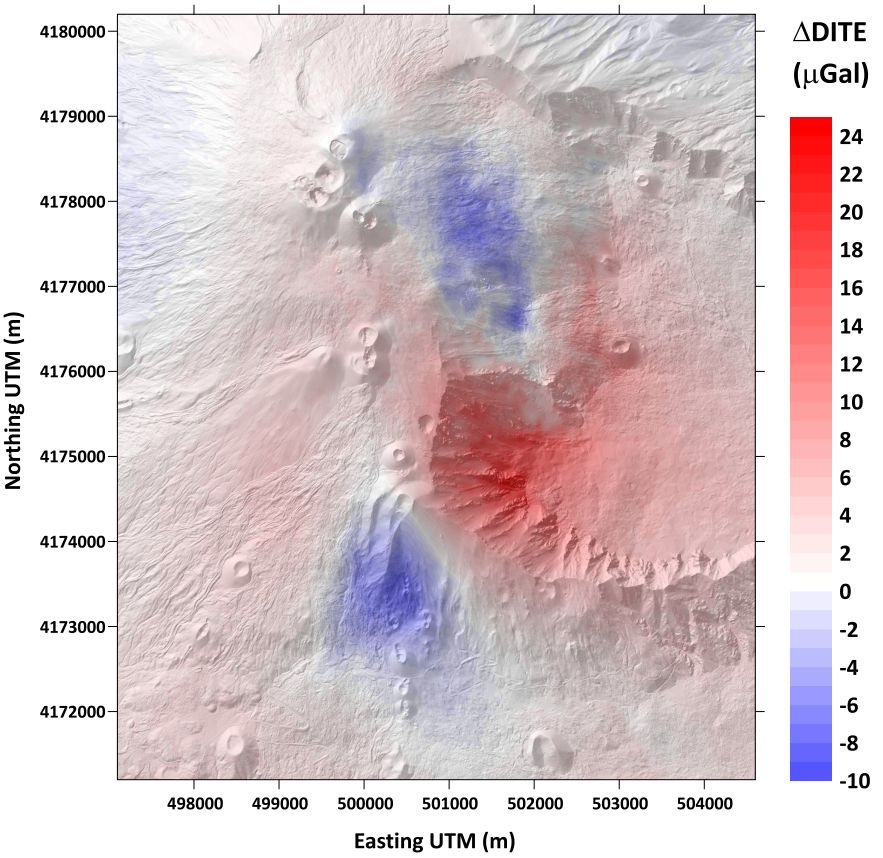

Fig. 6. The difference (μGal) between the DITE field and its normal-free-air approximation (nFAE) for the vertical displacement field shown in Fig. 2.

normal-free-air (nFAE) approximation of DITE, cf. Eq. (6). Over the whole study area the statistics of the difference between the two fields are: min = $-9.2\ \mu$Gal, max = $23.5\ \mu$Gal, mean = $3.2\ \mu$Gal, and RMS = $5.1\ \mu$Gal.

In Figure 7 we show the difference of Figure 6 in a relative sense as this difference divided by the DITE. We do this only for the grid (mesh) points where the DITE signal (in absolute sense) is greater than $5\ \mu$Gal, to avoid values of several hundred percent for spots where the DITE is very small. This relative difference is interpolated over the empty spots where the DITE signal (in absolute sense) is less than $5\ \mu$Gal.

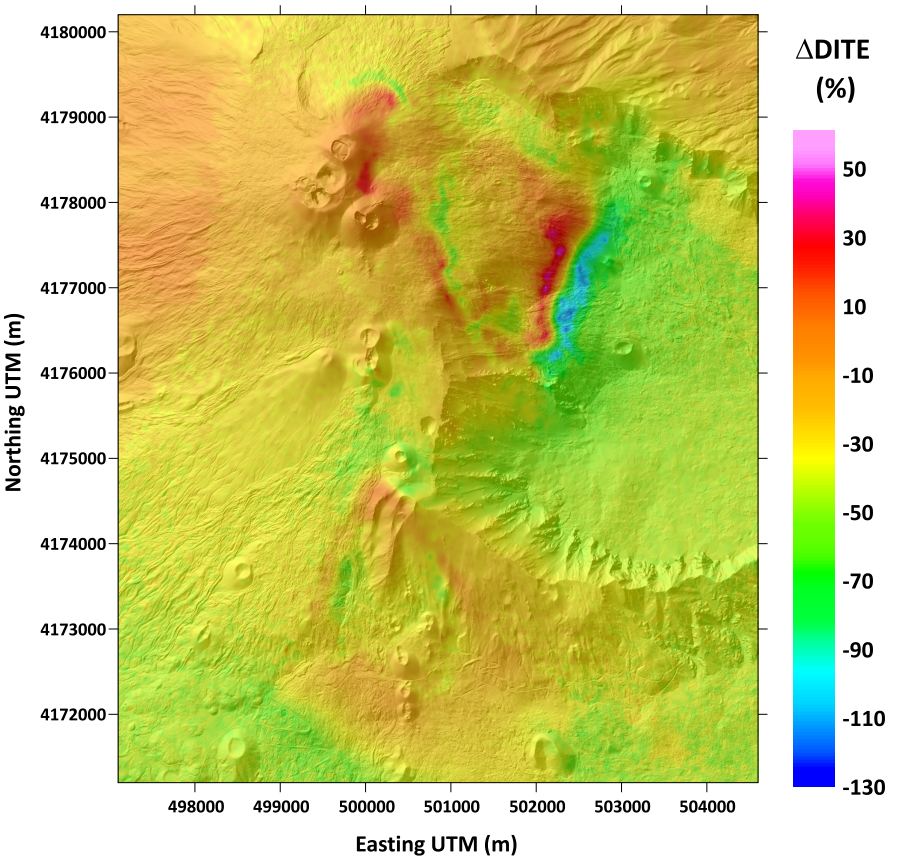

Fig. 7. The difference shown in Fig. 6 presented in relative sense (%).

2.6. Comparison of DITE and the vertical displacement field multiplied by topographically predicted VGG field

As a matter of interest we compare (Fig. 9) with the DITE field also the gravitational effect computed as the vertical displacement field multiplied by the topographically predicted VGG field (Eq. (7)). For this purpose we make use of the topographically predicted VGG field (*Vajda et al., 2020*) shown in Fig. 8. It approximates, for the sake of our comparison, the true (in-situ) VGG field.

In Figure 10 we show the difference of Figure 9 in a relative sense as this difference divided by the DITE. We do this only for the grid (mesh)

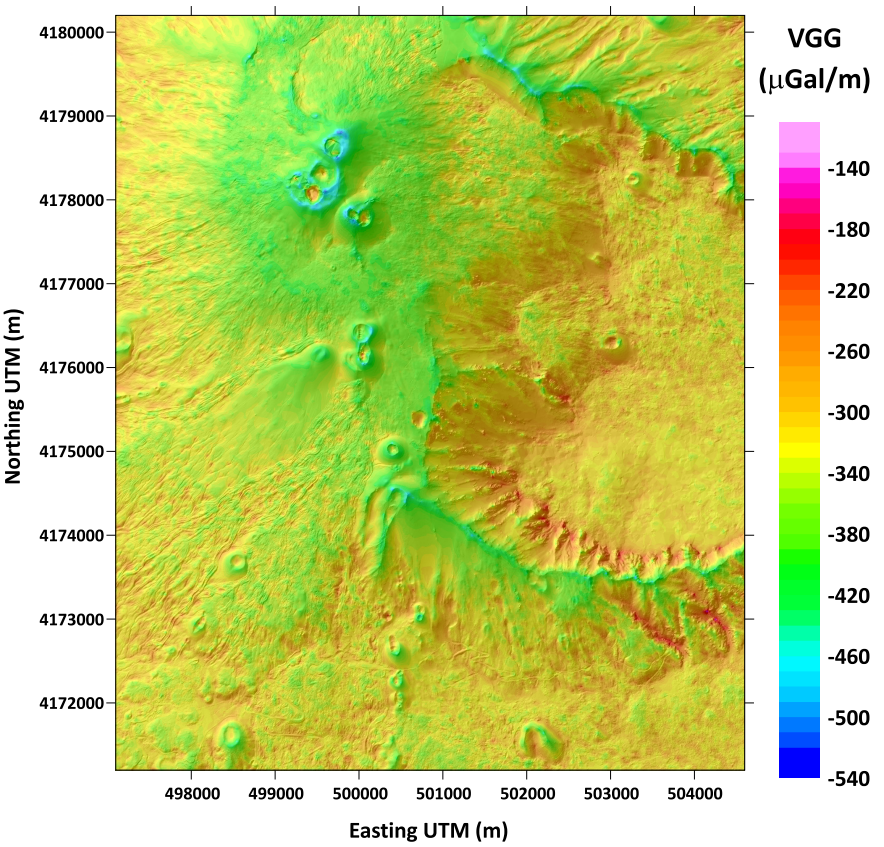

Fig. 8. The topographically predicted VGG field (μGal/m) draped over shaded relief in our study area.

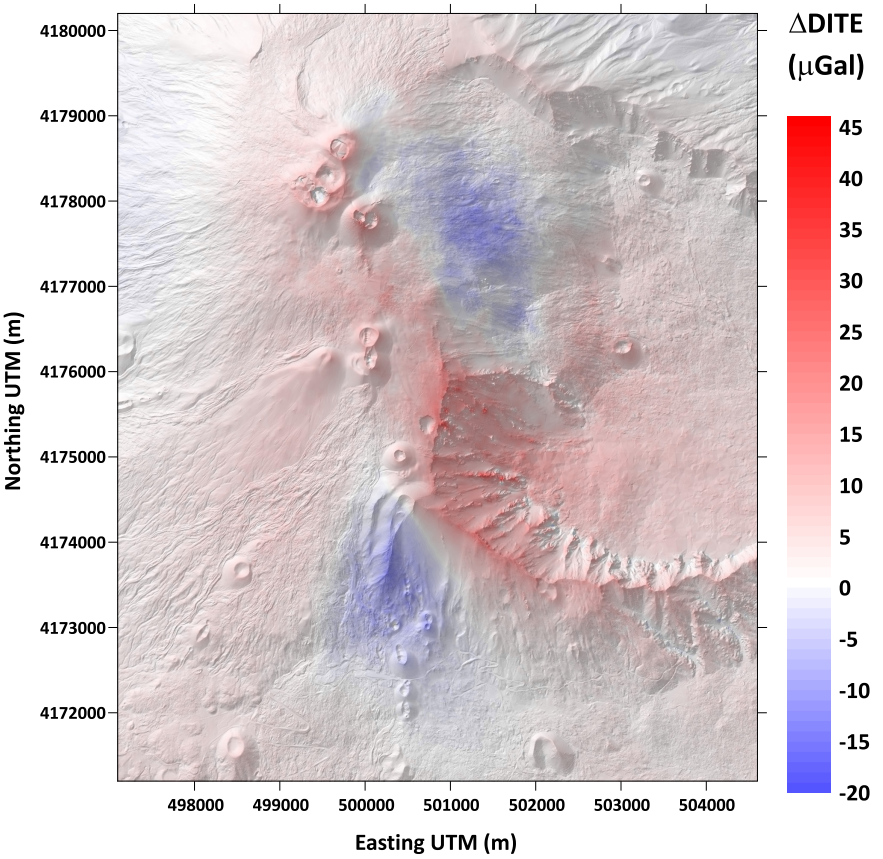

Fig. 9. The difference (μGal) between the DITE field and the field given by Eq. (7) based on the topographically predicted VGG field, for the vertical displacement field shown in Fig. 2.

points where the DITE signal (in absolute sense) is greater than 5 μGal, to avoid values of several hundred percent for spots where the DITE is very small. This relative difference is interpolated over the empty spots where the DITE signal (in absolute sense) is less than 5 μGal.

3. Discussion

Numerical simulations (*Vajda et al., 2019*) of DITE fields based on synthetic deformation fields of various lateral extents and shapes imposed over var-

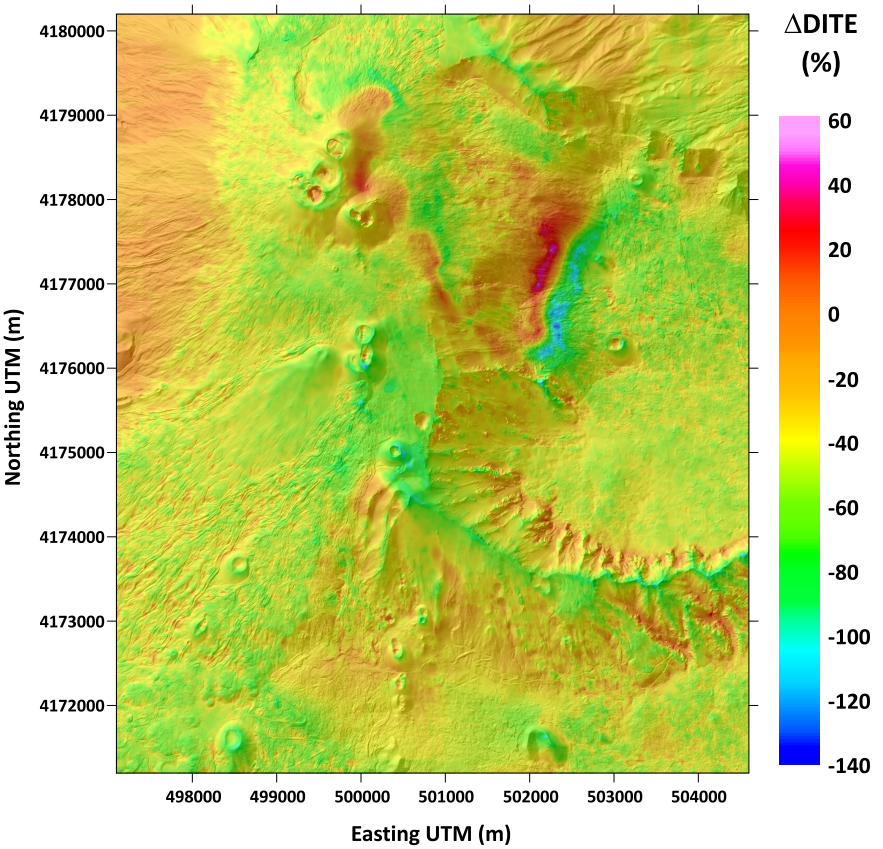

Fig. 10. The difference shown in Fig. 9 presented in relative sense (%).

ious features of volcanic relief revealed that the physical nature of DITE varies between two limiting cases: the nFAE-DITE and the BCFAG-DITE. The DITE varies depending on the shape, lateral extent and amplitude of the deformation field, as well as the shape of the relief over which it is imposed. In flatter or less rugged relief and for widespread fairly monotonous deformation fields the nature of DITE is closer to its Bouguer representation (Eq. (5)). In a special case of narrow spiky deformation fields (such as those generated by shallow small spherical sources) imposed over steep cone-shape terrain, the nature of DITE is closer to its normal-free-air (nFAE) representation (Eq. (6)). Here we set forth to examine what would be the situation with a surface deformation field generated by a relatively thin, vertically

elongated and relatively shallow source, such as a shallow dyke, in a morphological setting like that of the summit area on Etna.

The comparison of the Bouguer and nFAE fields approximating the DITE (qeDITE) field (sections 2.4 and 2.5) revealed that – for the whole study area (Etna summit area) – the nature of the DITE field due to the dyke intrusion related to the Dec-2018 Etna fissure eruption dwells somewhere inbetween the Bouguer and nFAE representations. Although, from the viewpoint of the whole study area, the Bouguer approximation performs slightly better than the normal-FAE approximation (cf. Table 1), neither of them is accurate enough in the whole summit area of Etna (cf. Figs. 4 and 6 as well as 5 and 7).

However, the situation reverses when focusing on the four summit craters. Over the summit craters the deviation of the Bouguer approximation reaches 10 to 15 μGal (25 to 50% of the DITE signal, in relative sense), while the deviation of the nFAE approximation is negligible (at the level of a couple of μGals). Thus, over the summit craters the DITE would be most properly approximated by the nFAE, while in some other parts of the Etna summit area the Bouguer approximation would perform better.

Table 1. Statistics of the deviations ("dev") of the three fields from the DITE (μGal) over our study area.

statistics	BCFAG-DITE dev	nFAE-DITE dev	pVGG*dh dev
min	−14.5	−9.2	−18.2
max	7.5	23.5	45.5
mean	−1.1	3.2	4.0
RMS	2.3	5.1	6.2

In addition we compared to the DITE (qeDITE) field also the field computed as the product of the vertical displacement field and the topographically predicted VGG field (section 2.6), purely out of curiosity, to see if it could potentially serve as an appropriate approximation of the DITE. It turns out (cf. last column in Table 1 and Figs. 9 and 10) that it would not be a good approximation of DITE.

4. Conclusions

In our presented study we do not deal with explaining the source of the

Dec-2018 paroxysmal eruption on Etna from observed deformation or gravity changes. We use the syn-eruptive surface deformation field observed by the SAR satellite technology only as a means for computing the deformation-induced topographic effect (DITE) related to the inferred source (*Bonforte et al., 2019; De Novellis et al., 2019; Aloisi et al., 2020*), a "double dyke" with a shallow dyke intrusion leading to a fissure eruption. We focus here on studying the character of the DITE field generated by such shallow dykes on reliefs such as that of the Etna summit area, and examine the options of approximating such DITE properly in case when the surface vertical displacement field is not available in areal (grid) form, only in discrete form as elevation changes at gravity benchmarks.

Based on this case study we come to the conclusion that in situations with surface deformation fields of similar character (generated by relatively shallow vertically elongated intrusions such as nearly vertical dykes) in areas with terrain reliefs similar to the summit area of Etna, neither the Bouguer nor the normal-FAE approximation of the DITE is accurate enough. Consequently, two types of residual gravity changes should be computed in such situations. One, in which the observed gravity changes are corrected for the gravitational effect of surface deformation by multiplying the elevation changes at benchmarks by the BCFAG (Eq. (5)), and the other, in which the elevation changes are multiplied by the constant theoretical (normal) FAG (Eq. (6)). Then, both types of residual gravity changes should be inverse-modelled and interpreted, yielding the two marginal source solutions, whereby the more realistic solution can be expected somewhere inbetween the two.

Multiplying the elevation changes at benchmarks by the in-situ (observed), or topographically predicted VGG values at benchmarks, does not appear to be a viable alternative for approximating the DITE. We are not analysing here whether it would be a good approximation of the deformation-induced effect (DIE) which includes also the gravitational effect of inner deformations (cf. *Vajda et al., 2019*). We focus solely on DITE and its approximations. In the context of volcano gravimetry, we recommend to exercise all effort to obtain the vertical displacement field accompanying the spatiotemporal gravity changes in areal form, and compute the DITE by numerical realization of Eq. (4).

Acknowledgements. This work was partially supported by the Slovak Research and Development Agency under contracts (projects) APVV-19-0150 (acronym ALCABA) and APVV- 16-0482 (acronym LITHORES), as well as by the VEGA grant agency under projects 2/0006/19 and 2/0100/20.

References

Aldeghi A., Carn S., Escobar-Wolf R., Groppelli G., 2019: Volcano Monitoring from Space Using High-Cadence Planet CubeSat Images Applied to Fuego Volcano, Guatemala. Remote Sens., **11**, 18, 2151, doi: 10.3390/rs11182151.

Aloisi M., Bonaccorso A., Cannavò F., Currenti G., Gambino S., 2020: The 24 December 2018 eruptive intrusion at Etna volcano as revealed by multidisciplinary continuous deformation networks (CGPS, borehole strainmeters and tiltmeters). J. Geophys. Res. Solid Earth, **125**, 8, e2019JB019117, doi: 10.1029/2019JB019117.

Alparone S., Barberi G., Giampiccolo E., Maiolino V., Mostaccio A., Musumeci C., Scaltrito A., Scarfì L., Tuvè T., Ursino A., 2020: Seismological constraints on the 2018 Mt. Etna (Italy) flank eruption and implications for the flank dynamics of the volcano. Terra Nova, **32**, 5, 334–344, doi: 10.1111/ter.12463.

Battaglia M., Gottsmann J., Carbone D., Fernández J., 2008: 4D volcano gravimetry. Geophysics, **73**, 6, WA3–WA18, doi: 10.1190/1.2977792.

Berrino G., Corrado G., Luongo G., Toro B., 1984: Ground deformation and gravity changes accompanying the 1982 Pozzuoli uplift. Bull. Volcanol., **47**, 2, 187–200, doi: 10.1007/BF01961548.

Berrino G., Rymer H., Brown G. C., Corrado G., 1992: Gravity-height correlations for unrest at calderas. J. Volcanol. Geotherm. Res., **53**, 1-4, 11–26, doi: 10.1016/0377-0273(92)90071-K.

Bisson M., Spinetti C., Neri M., Bonforte A., 2016: Mt. Etna volcano high-resolution topography: airborne LiDAR modelling validated by GPS data. Int. J. Digit. Earth, **9**, 7, 710–732, doi: 10.1080/17538947.2015.1119208.

Bonaccorso A., Bonforte A., Currenti G., Del Negro C., Di Stefano A., Greco F., 2011: Magma storage, eruptive activity and flank instability: Inferences from ground deformation and gravity changes during the 1993–2000 recharging of Mt. Etna volcano. J. Volcanol. Geotherm. Res., **200**, 3-4, 245–254, doi: 10.1016/j.jvolgeores.2011.01.001.

Bonaccorso A., Giampiccolo E., 2020: Balance Between Deformation and Seismic Energy Release: The Dec 2018 'Double-Dike' Intrusion at Mt. Etna. Front. Earth Sci., **8**, 583815, doi: 10.3389/feart.2020.583815.

Bonforte A., Fanizza G., Greco F., Matera A., Sulpizio R., 2017: Long-term dynamics across a volcanic rift: 21 years of microgravity and GPS observations on the southern flank of Mt. Etna volcano. J. Volcanol. Geotherm. Res., **344**, 174–184, doi: 10.1016/j.jvolgeores.2017.06.005.

Bonforte A., Guglielmino F., Puglisi G., 2019: Large dyke intrusion and small eruption: The December 24, 2018 Mt. Etna eruption imaged by Sentinel-1 data. Terra Nova, **31**, 4, 405–412, doi: 10.1111/ter.12403.

Calvari S., Bilotta G., Bonaccorso A., Caltabiano T., Cappello A., Corradino C., Del Negro C., Ganci G., Neri M., Pecora E., Salerno G. G., Spampinato L., 2020: The VEI 2 Christmas 2018 Etna eruption: A small but intense eruptive event or the starting phase of a larger one? Remote Sens., **12**, 6, 905, doi: 10.3390/rs12060905.

Cannavò F., 2019: A new user-friendly tool for rapid modelling of ground deformation. Comput. Geosci., **128**, 60–69, doi: 10.1016/j.cageo.2019.04.002.

Cannavò F., Sciotto M., Cannata A., Di Grazia G., 2019: An integrated geophysical approach to track magma intrusion: The 2018 Christmas Eve eruption at Mount Etna. Geophys. Res. Lett., **46**, 8009–8017, doi: 10.1029/2019GL083120.

Carbone D., Poland M. P., Diament M., Greco F., 2017: The added value of time-variable microgravimetry to the understanding of how volcanoes work. Earth-Sci. Rev., **169**, 146–179, doi: 10.1016/j.earscirev.2017.04.014.

Carr B. B., Clarke A. B., Arrowsmith J. R., Vanderkluysen L., Dhanu B. E., 2019: The emplacement of the active lava flow at Sinabung Volcano, Sumatra, Indonesia, documented by structure-from-motion photogrammetry. J. Volcanol. Geotherm. Res., **382**, 164–172, doi: 10.1016/j.jvolgeores.2018.02.004.

Chauhan M. S., Cannavó F., Carbone D., Greco F., 2020: Insights into Mount Etna December 2018 eruption from joint inversion of deformation and gravity data. Geophys. Res. Lett., **47**, 16, e2020GL087786, doi: 10.1029/2020GL087786.

Chen C. W., Zebker H. A., 2000: Network approaches to two-dimensional phase unwrapping: intractability and two new algorithms. J. Opt. Soc. Am. A, **17**, 3, 401–414, doi: 10.1364/JOSAA.17.000401.

De Novellis V., Atzori S., De Luca C., Manzo M., Valerio E., Bonano M., Cardaci C., Castaldo R., Di Bucci D., Manunta M., Onorato G., Pepe S., Solaro G., Tizzani P., Zinno I., Neri M., Lanari R., Casu F., 2019: DInSAR analysis and analytical modeling of Mount Etna displacements: The December 2018 volcano-tectonic crisis. Geophys. Res. Lett., **46**, 11, 5817–5827, doi: 10.1029/2019GL082467.

Diefenbach A. K., Crider J. G., Schilling S. P., Dzurisin D., 2012: Rapid, low-cost photogrammetry to monitor volcanic eruptions: An example from Mount St. Helens, Washington, USA. Bull. Volcanol., **74**, 2, 579–587, doi: 10.1007/s00445-011-0548-y.

Diefenbach A. K., Bull K. F., Wessels R. L., McGimsey R. G., 2013: Photogrammetric monitoring of lava dome growth during the 2009 eruption of Redoubt Volcano. J. Volcanol. Geotherm. Res., **259**, 308–316, doi: 10.1016/j.jvolgeores.2011.12.009.

Fernández J., Pepe A., Poland M. P., Sigmundsson F., 2017: Volcano Geodesy: Recent developments and future challenges. J. Volcanol. Geotherm. Res., **344**, 1–12, doi: 10.1016/j.jvolgeores.2017.08.006.

Fornaciai A., Behncke B., Favalli M., Neri M., Tarquini S., Boschi E., 2010: Detecting short-term evolution of Etnean scoria cones: a LIDAR-based approach. Bull. Volcanol., **72**, 10, 1209–1222, doi: 10.1007/s00445-010-0394-3.

Greco F., Currenti G., D'Agostino G., Germak A., Napoli R., Pistorio A., Del Negro C., 2012: Combining relative and absolute gravity measurements to enhance volcano monitoring. Bull. Volcanol., **74**, 7, 1745–1756, doi: 10.1007/s00445-012-0630-0.

Hayford J. F., Bowie W., 1912: The effect of topography and isostatic compensation upon the intensity of gravity. U.S. Coast and Geodetic Survey, Washington, D.C., Special Publication No. 10.

Jordan B. R., 2019: Collecting field data in volcanic landscapes using small UAS (sUAS)/ drones. J. Volcanol. Geotherm. Res., **385**, 231–241, doi: 10.1016/j.jvolgeores.2019.07.006.

Ketelaar V. B. H. G., 2009: Satellite Radar Interferometry: Subsidence Monitoring Techniques. Springer, Netherlands, 244 p., ISBN 978-1-4020-9428-6, doi: 10.1007/978-1-4020-9428-6.

Laiolo M., Ripepe M., Cigolini C., Coppola D., Schiava M. D., Genco R., Innocenti L., Lacanna G., Marchetti E., Massimetti F., Silengo M. C., 2019: Space- and ground-based geophysical data tracking of magma migration in shallow feeding system of Mount Etna volcano. Remote Sens., **11**, 10, 1182, doi: 10.3390/rs11101182.

Miller C. A., Le Mével H., Currenti G., Williams-Jones G., Tikoff B., 2017: Microgravity changes at the Laguna del Maule volcanic field: Magma-induced stress changes facilitate mass addition. J. Geophys. Res. Solid Earth, **122**, 4, doi: 10.1002/2017JB014048.

Okyay U., Telling J., Glennie C. L., Dietrich W. E., 2019: Airborne lidar change detection: An overview of Earth sciences applications. Earth-Sci. Rev., **198**, 102929, doi: 10.1016/j.earscirev.2019.102929.

Rymer H., 1994: Microgravity change as a precursor to volcanic activity. J. Volcanol. Geotherm. Res., **61**, 3-4, 311–328, doi: 10.1016/0377-0273(94)90011-6.

Schiavone D., Loddo M., 2007: 3-D density model of Mt. Etna Volcano (Southern Italy). J. Volcanol. Geotherm. Res., **164**, 3, 161–175, doi: 10.1016/j.jvolgeores.2007.04.016.

Vajda P., Zahorec P., Bilčík D., Papčo J., 2019: Deformation-induced topographic effects in interpretation of spatiotemporal gravity changes: Review of approaches and new insights. Surv. Geophys., **40**, 5, 1095–1127, doi: 10.1007/s10712-019-09547-7.

Vajda P., Zahorec P., Papčo J., Carbone D., Greco F., Cantarero M., 2020: Topographically predicted vertical gravity gradient field and its applicability in 3D and 4D microgravimetry: Etna (Italy) case study. Pure Appl. Geophys., **177**, 7, 3315–3333, doi: 10.1007/s00024-020-02435-x.

Vajda P., Zahorec P., Miller C. A., Le Mével H., Papčo J., Camacho A. G., 2021: Novel treatment of the deformation–induced topographic effect for interpretation of spatiotemporal gravity changes: Laguna del Maule (Chile). J. Volcanol. Geotherm. Res., **414**, 107230, doi: 10.1016/j.jvolgeores.2021.107230.

Van Camp M., de Viron O., Watlet A., Meurers B., Francis O., Caudron C., 2017: Geophysics from terrestrial time-variable gravity measurements. Rev. Geophys., **55**, 4, 938–992, doi: 10.1002/2017RG000566.

Zahorec P., Vajda P., Papčo J., Sainz-Maza S., Pereda de Pablo J., 2016: Prediction of vertical gradient of gravity and its significance for volcano monitoring – Example from Teide volcano. Contrib. Geophys. Geod., **46**, 3, 203–220, doi: 10.1515/congeo-2016-0013.

Zahorec P., Marušiak I., Mikuška J., Pašteka R., Papčo J., 2017: Chapter 5 – Numerical Calculation of Terrain Correction Within the Bouguer Anomaly Evaluation (Program Toposk). 79–92. In: Pašteka R., Mikuška J., Meurers B. (Eds.): Understanding the Bouguer Anomaly: A Gravimetry Puzzle, Elsevier, ISBN 978-0-12-812913-5, doi: 10.1016/B978-0-12-812913-5.00004-X.